ADVANCED MATERIALS
www.advmat.de

Continuous-Wave Pumped Self-Assembled Colloidal Topological Lasers

Rui Duan, Qiang Zhang, Yi Tian Thung, Xuehong Zhou, Tingting Yin, Yutian Ao, Lian Xiao, Zitong Zhang, Calvin Xiu Xian Lee, Tianhua Ren, Hilmi Volkan Demir, Wen Siang Lew, Baile Zhang,* and Handong Sun**

The field of optoelectronic integrated circuits is actively developing reliable and efficient room-temperature continuous-wave (CW) lasers. CW-pumped lasers combine the economical and simple manufacturing processes of colloidal semiconductor lasers with the efficient and stable output of continuous pumping, enabling them to significantly impact the field of semiconductor lasers. However, development is still severely challenged by limitations such as gain materials and cavity structures. Consequently, as a compromise, most colloidal semiconductor lasers proposed to date have relied on another pulsed laser as the pumping source. In this study, a self-assembled colloidal topological laser is proposed that benefits from CW pumping at room temperature. By utilizing an interfacial self-assembly strategy, nanoplatelets (NPLs) are managed to control the collective orientation (face-down or edge-up), achieving controlled polarization of amplified spontaneous emission for the first time. Furthermore, precise control over the thickness of a single NPL layer is demonstrated, which enables the laser system to offer extensive wavelength tunability (over 50 nm), ultra-high polarization (over 95%), and good temporal stability. These metrics signify the optimal performance level of colloidal semiconductor lasers, marking a new era in solution processing systems for the optoelectronic integrated circuit field.

1. Introduction

Colloidal nanoplatelets (NPLs) are an exceptionally promising new type of luminescent material, considered as candidates for the next generation of laser gain media. Among all the solution-processable gain materials studied so far for lasing applications, colloidal NPLs stand out for their suppressed nonradiative Auger recombination rates compared to zerodimensional (0D) quantum dots and one-dimensional (1D) nanorods.[1–5] More importantly, colloidal NPLs can self-assemble, achieving nanoscale precise control of stacking thickness and collective orientation.[6–8] Recent studies have demonstrated that the self-assembly of NPLs can significantly enhance the emission performance of optoelectronic devices.[2,9,10] For instance, by aligning the transition dipole moments of NPLs parallel to their surface through self-assembly, the external quantum efficiency of light-emitting diodes (LEDs) can be effectively

R. Duan, T. Ren, H. Sun
Institute of Applied Physics and Materials Engineering
University of Macau
Macao SAR 999078, China
E-mail: hdsun@um.edu.mo

Q. Zhang
Nanophotonics Research Center
Shenzhen Key Laboratory of Micro-Scale Optical Information Technology
Institute of Microscale Optoelectronics
Shenzhen University
Shenzhen 518060, China
E-mail: zhangqiang@szu.edu.cn

The ORCID identification number(s) for the author(s) of this article can be found under https://doi.org/10.1002/adma.202416635

DOI: 10.1002/adma.202416635

Y. T. Thung, X. Zhou, T. Yin, Y. Ao, L. Xiao, C. X. X. Lee, H. V. Demir, W. S. Lew, B. Zhang
Division of Physics and Applied Physics
School of Physical and Mathematical Sciences
Nanyang Technological University
21 Nanyang Link, Singapore 637371, Singapore
E-mail: blzhang@ntu.edu.sg

Y. T. Thung, H. V. Demir
LUMINOUS! Centre of Excellence for Semiconductor Lighting and Displays
The Photonics Institute
School of Electrical and Electronic Engineering
Nanyang Technological University
Singapore 639798, Singapore

Z. Zhang
Institute of Semiconductors
Guangdong Academy of Sciences
Guangzhou, Guangdong 510650, China

H. V. Demir
Department of Electrical and Electronics Engineering
Department of Physics
UNAM-Institute of Materials Science and Nanotechnology and the National Nanotechnology Research Center
Bilkent University
Ankara 06800, Türkiye

increased by more than 50%.[9] Furthermore, meticulous control of the collective orientation of NPLs enables the attainment of direct linearly polarized electroluminescence in the absence of any photonic structures.[10] Colloidal NPLs also exhibit a range of impressive characteristics crucial for laser applications, such as ultranarrow emission line width,[11–13] giant oscillator strength,[14,15] giant linear and nonlinear absorption cross-sections,[11,13] and large modal optical gain coefficients.[16] These attributes position colloidal NPLs as ideal candidates for the next generation of micro- and nano-lasers. Despite rapid advances in low-threshold lasers and device miniaturization, the performance of colloidal semiconductor lasers still falls significantly short of expectations. To achieve electric drive, continuous-wave (CW) optically pumped lasers are not only an essential path to this objective but also signify a critical technological breakthrough. Nevertheless, the resolution of the CW pumping issue for colloidal semiconductor lasers at room temperature is still in its absolute nascent stages, with significant potential for improvement in areas such as lasing threshold, quality factor, and wavelength tunability.[4,5,17,18] The key to overcoming these challenges hinge on the meticulous optimization of the gain medium and the laser cavity.

Topological photonics introduces innovative excitation mechanisms to micro- and nano- lasers, enabling the design of robust light flows within compact cavity structures.[19,20] In recent developments, researchers have harnessed the attributes of topological protection, effectively integrating gain materials into topological photonic structures.[21–28] This breakthrough paves the way for the creation of top-tier topological lasers with exceptional performance capabilities. However, the majority of existing topological lasers rely on either 1D chains[22]or twodimensional (2D) arrays of semiconductor resonators,[21,25,26,29] with their emission primarily at the edges or corners, predominantly in the infrared spectrum. Developing topological lasers emitting within the visible light spectrum poses substantial challenges. A practical obstacle is that the photonic structure dimensions required for achieving topological lasers within the visible spectrum are typically on the nanometer scale. This demands extremely high manufacturing precision and relies on cutting-edge nanofabrication technologies (typically electron-beam lithography). These cumbersome and costly manufacturing processes limit the large-scale production of topological lasers. Therefore, developing a high-performance topological laser that does not require complex lithographic patterning and has a simpler fabrication process is a crucial direction for current research.

In this work, we overcome these pressing challenges, pioneering the development of a CW optically pumped self-assembled colloidal topological laser, which is demonstrated for the first time using colloidal nanocrystals (**Figure 1**a). To accomplish this, we focus on addressing the following key factors. First, we synthesize heterogeneous colloidal NPLs that exhibit high uniformity and enhanced gain properties, essential for the generation of high-performance lasers. Second, a topological vertical-cavity is designed, which can be fabricated without the need for complex and expensive lithographic techniques. Third, the self-assembly of colloidal NPLs is managed to control the collective orientation and stacking thickness of the NPLs, achieving nanoscale control over the topological cavities. For the first time, we have achieved controllable modulation of the polarization properties of amplified spontaneous emission in colloidal nanocrystal lasers. Additionally, our self-assembled colloidal topological laser exhibit extensive wavelength tunability (>50 nm), ultra-high polarization (> 95%), ultra-high-quality factor (≈11 800) and good temporal stability, all achieved through CW pumping at room temperature.

2. Results and Discussion

2.1. Optical Properties and Self-Assembly of CdSe Colloidal NPLs

The red-emitting CdSe/CdS@$Cd_{1-x}Zn_xS$ core/buffer-shell@graded-shell NPLs as the gain material were synthesized (for detailed synthesis procedures, please refer to Supporting Information Experimental Section). The $Cd_{1-x}Zn_xS$ graded shell offers robust type-I confinement on photoexcited carriers, effectively enhancing the overlap of their wavefunctions. This helps to mitigate excitonic interactions with surface defects, resulting in exceptional optical gain characteristics. The buffer and graded shell layers also aid in diminishing interfacial defects between the core and shell components of the NPLs. This reduction in interfacial defects, consequently, helps suppress significant Auger recombination when momentum conservation is relaxed due to a decreased interfacial potential between the core and shell components. These enhancements guarantee a high photoluminescence quantum yield (PLQY) and a narrow emission line width, both of which are highly desirable traits for laser operation.

The colloidal NPL solution possesses high monodispersity and size uniformity, emitting photoluminescence (PL) of 654 nm with a narrow full-width half-maximum (FWHM) of ≈21 nm, and a high PLQY of 99% (Figure S1a, Supporting Information). Closer examination under bright-field transmission electron microscopy (TEM) reveals that the NPLs exhibit atomic flatness, and possess a uniform rectangular shape (Figure S1b, Supporting Information). Time-resolved photoluminescence (TRPL) spectroscopy conducted on a film of NPLs (**Figure 2**a) unveils two emission bands to illustrate the spectral evolution from spontaneous emission to amplified spontaneous emission (ASE). During the early times, as indicated by the white dashed line in Figure 2a, the PL spectrum was effectively fitted by a two-peak Lorentzian function (Figure 2b), corresponding to single exciton and biexciton emissions. Based on the double-band deconvolution, the energy of the single exciton is 1.91 eV, and the biexciton binding energy E_b^{xx} is determined to be ≈37 meV from the energy separation between the peak positions. Given that the thermal energy of the ambient environment at 300 K is ≈26 meV, the higher value of E_b^{xx} allows for biexciton state to exist well beyond room temperature.[30] The substantial biexciton binding energy also induces a redshift in the stimulated emission peak away from the spontaneous emission peak, thereby minimizing reabsorption to achieve a low stimulated emission threshold. The gain characteristics of the as-synthesized NPLs are evaluated via their pump intensity-dependent PL using a variable stripe length (VSL) excitation geometry, as depicted in Figure 2c. As the pump power of quasi-continuous nanosecond pulses (532 nm, 1 ns, 60 Hz) increases, a distinctive, narrower emission band emerges on the red side of the spontaneous emission band to indicate the onset of ASE. Excitation intensity-dependent TRPL measurements were also performed on NPLs thin films before, close to, and after

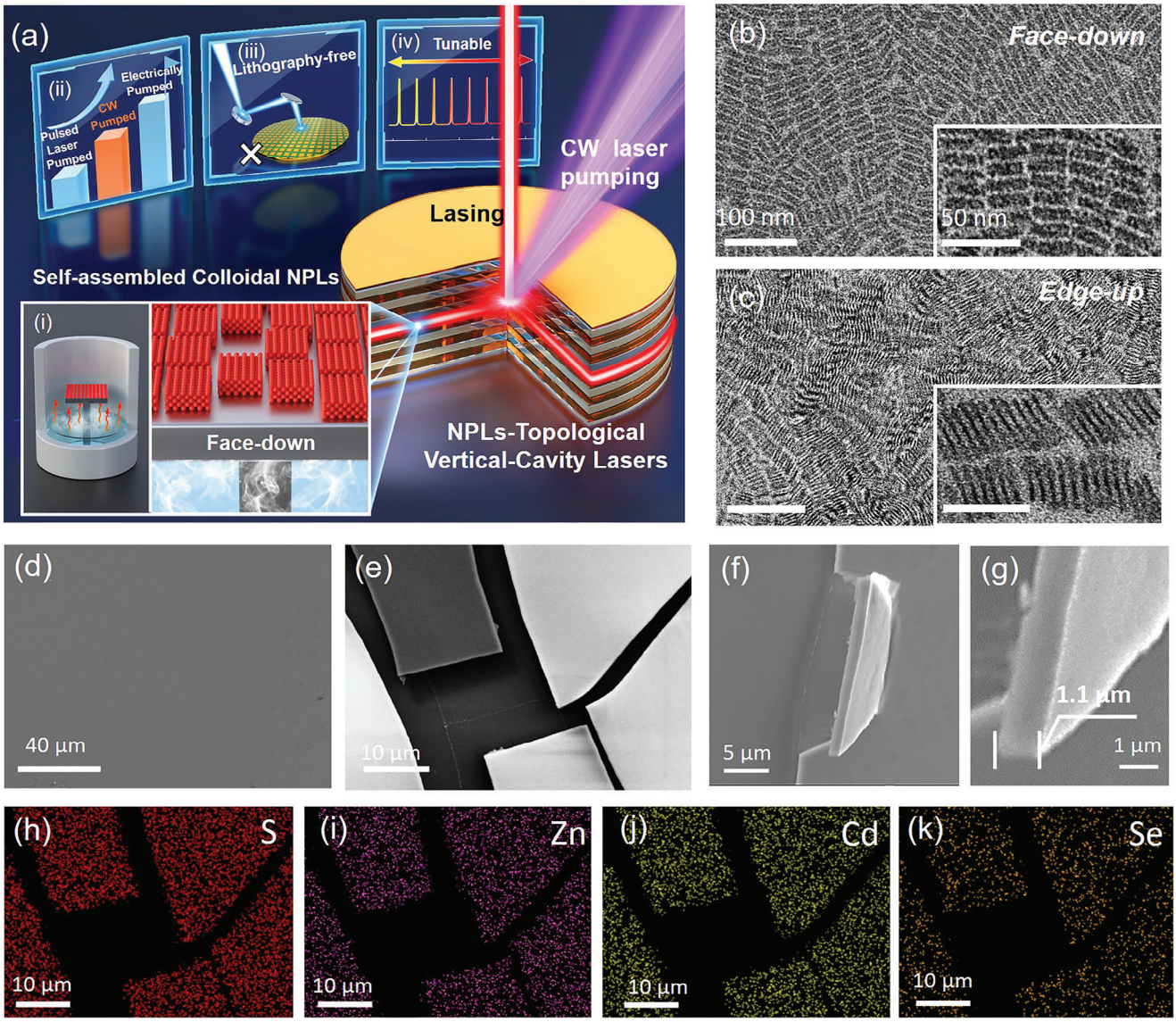

Figure 1. a) The schematic diagram of CW pumped self-assembled NPLs – topological laser at room temperature. Topological vertical-cavity was designed without the need for complex lithography. Inset i) concisely illustrates how an interfacial self-assembly strategy was employed to control the collective orientation of NPLs and integrate them into the topological vertical-cavity. Insets (ii–iv) highlight the advantages of the proposed topological laser, including CW pumping, lithography-free fabrication, and wide-range tunability. b,c) TEM images of NPLs showing face-down and edge-up assemblies, respectively. d,e) SEM images showcasing the uniformity and smoothness of the colloidal NPLs film. f) SEM image of the cracker from broken NPLs film. g) Detail of a fractured area, showing a film thickness of ≈1.1 µm. h–k) The elemental mapping of the NPLs film confirms that the fractured area shown in (e) is composed of NPLs.

the ASE threshold (Figure 2d; Table S1, Supporting Information). The inset of Figure 2c shows an unprecedented ultra-low threshold of Pth ≈3.8 µJ cm^{-2}, providing a high-gain foundation for the generation of stimulated emission under continuous-wave pumping.

Interfacial self-assembly strategy emerges as a potent tool for facilitating the formation of highly ordered superstructures in colloidal materials, thereby enabling the creation of superlattices in optoelectronic devices. For the first time, we have controlled the polarization characteristics of ASE by manipulating the orientation of colloidal NPLs. We adjusted the NPLs collective orientation (face-down or edge-up) at the interface by regulating the evaporation rate of the solvent, while avoiding the use of non-volatile insulating additives that could potentially impact device performance (please see Figure S2, Supporting Information for details). To more clearly demonstrate the face-down and edge-up configurations, we performed measurements using 4-monolayer (ML) CdSe NPLs as examples. Experimental findings indicate that employing a solvent with rapid evaporation (hexane) results in the formation of a kinetically trapped product, i.e., NPLs adopting a face-down configuration (Figures 1b, and 2e); conversely, employing a solvent with slow evaporation (octane) yields a thermodynamically favored product, i.e., NPLs assembling in an edge-up orientation (Figures 1c, and 2f).[8] As depicted

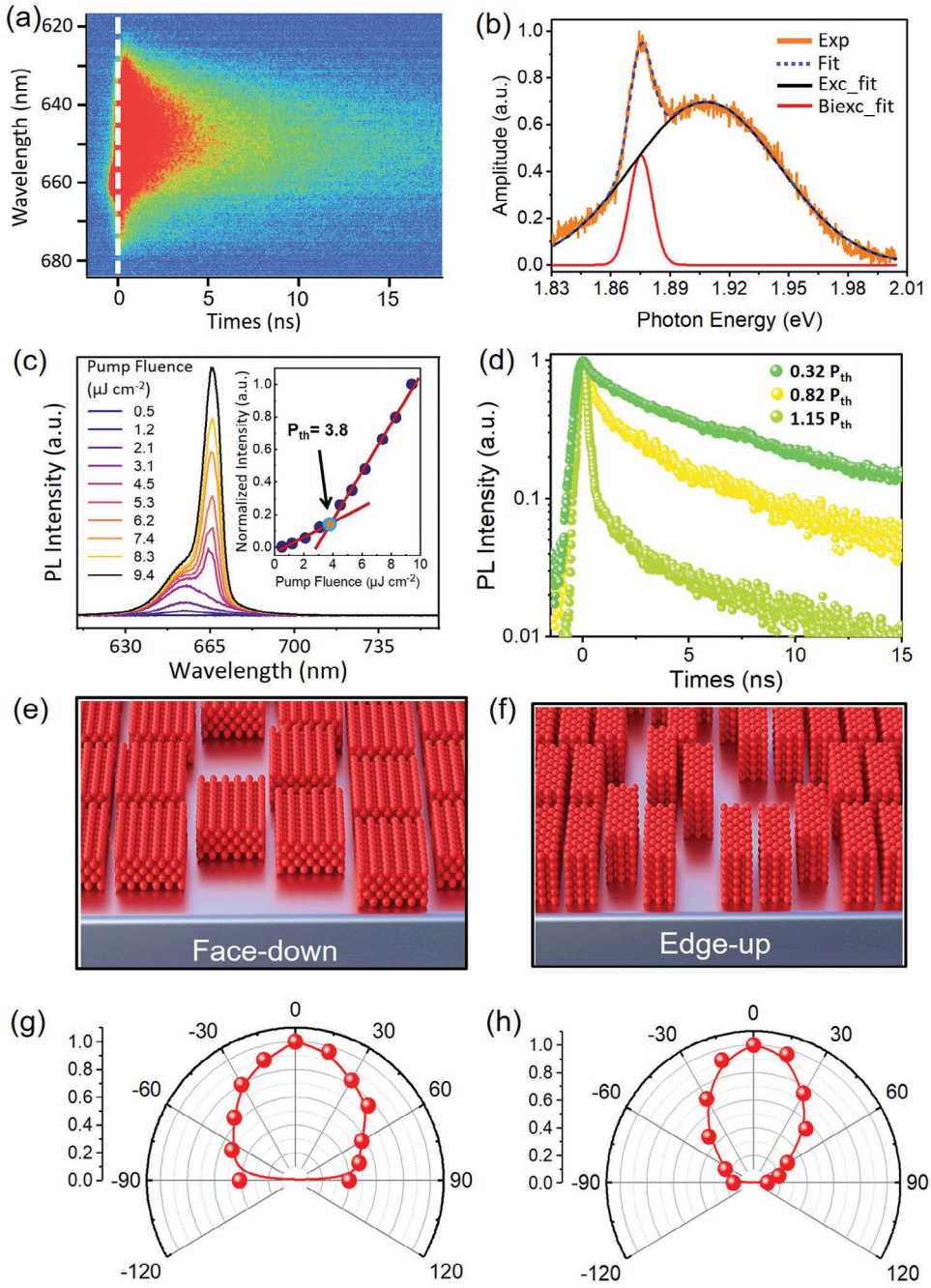

Figure 2. a) Streak camera image of the NPL film near ASE emission. The transition from blue to red in the spectrogram indicates a gradual increase in PL intensity. b) Early-time integrated intensity (orange line) of (a) panel along the white dashed line. The Lorentzian fitting of the single exciton and biexciton emissions are represented by the black and red line, respectively, with the composite fitting represented in blue. c) Excitation fluence dependence of PL emission under nanosecond excitation. The inset shows the normalized emission intensity with the pump fluences. d) Pump-intensity-dependent PL decay curves for NPLs film, at pump fluence before (≈0.32 Pth, ≈0.82 Pth) and after (≈1.15 Pth) the ASE threshold. The schematic diagram of the NPLs in collective orientation: face-down (e) and edge-up (f) configurations. Polar plot of ASE intensity versus detection polarization angle for NPLs, with face-down (g) and edge-up (h) configurations, respectively.

in Figure 2g,h the results indicate that the degree of polarization (DOP) of ASE for the face-down configuration was 0.43, while for the edge-up configuration, it reached as high as 0.81. The polarization properties exhibit significant discrepancies between the edge-up and face-down configurations. Results are apparent from the anisotropy of the dipole transition in NPLs. As shown in Figure S3 (Supporting Information), in the face-down configuration, the dipoles in the NPLs are orthogonally polarized along the x and y directions. Consequently, the overall isotropic state is ultimately exhibited. However, in the edge-up configuration, the

dipoles always align along the long axis in the plane of the NPLs, while the dipole transition perpendicular to the NPL plane is forbidden. As such, collecting emissions perpendicularly from the edges of the edge-up NPLs results in the observation of a highly polarized ASE output. In laser technology, unwanted polarized ASE inherently represents a loss mechanism. Interestingly, by managing the collective orientation of NPLs, we can control the polarization of ASE, thereby boosting the laser's performance.

2.2. Design of Topological Vertical-Cavity

We demonstrate how to integrate topological photonics with colloidal NPL systems. When two photonic crystals (PCs) with overlapping bandgaps come into contact, the topological interface states can be formed.[28,31] To investigate the influence of topological structure on lasing performance, we designed a topological vertical-cavity that exhibits this interface state, operating within the visible red and orange regions. Additionally, to elucidate the structure of topological vertical-cavity, comprehensive details are provided on the intricate design of the two types of photonic crystals that were engineered. Our approach to crafting a topological state within a binary photonic crystal (PC) draws on the classical 1D Su–Schrieffer–Heeger (SSH) model. The binary PC is constructed by alternating layers of low (SiO_2) and high (TiO_2) refractive indices, as shown in Figure S4 (Supporting Information), where the lower PC's (LPC) unit cell has its inversion center in the low refractive index layer, and the upper PC's (UPC) unit cell has its inversion center in the high refractive index layer. This particular design of topological vertical-cavities is mathematically equivalent to the SSH model,[32] where the LPC and UPC mimics the typical trivial and topological (non-trivial) 1D SSH lattice, respectively. In the tight binding approximation, the 1D SSH model Hamiltonian describing a 1D chain with two sites per unit cell and different intracell (v) and intercell (w) hopping amplitudes can be written as[33]

$$\hat{H} = \sum_n \left(v a_n^\dagger b_n + w b_{n-1}^\dagger a_n \right) + h.c. \quad (1)$$

where n represents the unit cells, $a_n^\dagger$ ($b_n^\dagger$) are the creation operators on the sublattice site a_n (b_n) in the nth unit cell, and $h.c.$ denotes the Hermitian conjugate. When the intracell hopping amplitude is larger than the intercell hopping amplitude, i.e., $v > w$, the lattice is trivial (left part in **Figure 3a**), while when $v < w$, the lattice is topological (right part in Figure 3a). The relevant band structures are plotted in Figure 3b,c. When v and w swap the value, the band structures are identical except for the topological edge states emerging in the gap at zero energy. The key topological characteristic of the band structure is the geometric phase, i.e., Zak phase θ, in 1D SSH model.[34] Specifically, in our design of the photonic crystals the Zak phase for the zeroth band (lowest band) can be calculated as:[35]

$$e^{i\theta} = \mathrm{sgn}\left(1 - \frac{\epsilon_A}{\epsilon_B}\right) \quad (2)$$

where ϵ_A (ϵ_B) represents the relative permittivity of the center (side) layer in the unit cell. Thus, LPC and UPC have Zak phase of 0 and π, respectively. The topological phases can also be revealed by the topological quantum number, i.e., the winding number, which is calculated by the Zak phase divided by π. The LPC is trivial with winding number 0, while the UCP is topologically nontrivial with winding number 1. Two degenerate edge states emerge at two boundaries of the topological lattice. When the trivial lattice and topological lattice are put in contact, the edge state emerges at the interface. With the help of topological stability, SiO_2 layer at the interface is replaced by the NPLs with different thickness to overlap the gain medium with the topological mode (Figure S4, Supporting Information). The opposite spatial distribution symmetries of the electric field are another representative discrepancy for these different topological states (Figure S5, Supporting Information).

2.3. Higher-Order Fabry–Pérot (FP) Mode in Topological Cavity

To thoroughly explore the laser characteristics, the thickness dependence of NPLs was investigated, ranging from several micrometers to tens of nanometers. Scanning Electron Microscope (SEM) images presented in Figure 1d,e effectively display the surface morphology of the colloidal NPLs films that were prepared. The uniformity of these NPL films is crucial for maintaining consistent optical gain within the resonator, significantly reducing the potential for mode competition and instability. Additionally, the smooth surface of these films minimizes surface scattering losses inside the cavity, thereby improving the Q-factor and concurrently lowering the lasing threshold. Figure 1h–k display the elemental mapping of the NPLs film, confirming that the fractured area shown in Figure 1e consists of NPLs. Figure 3d shows the laser signal from a topological cavity with an NPLs thickness of ≈14.5 µm. It is noteworthy that at this micrometer-scale thickness, the resonance mode transitions from a topological mode to a higher-order FP mode. The threshold for this NPLs lasers was determined to be as low as ≈21.6 W cm^{-2}. Furthermore, the emission linewidth's contraction served as a definitive indication of lasing action, as shown in Figure 3e. As depicted in Figure 3f, the multimode laser exhibits free spectral ranges ($FSRs$) at diverse intervals: ≈8.9, ≈12.2, and ≈20.7 nm. Remarkably, reducing the NPL layer's thickness to 1.1 µm (Figure 1g) enables single-mode lasing, as highlighted in Figure 3g, featuring an exceptionally narrow FWHM of ≈0.057 nm. This achievement not only signifies the creation of a single-mode laser with a high Q-factor estimated at ≈11 800, but also sets a new record for Q-factor values using colloidal NPLs, as detailed in Table S2 (Supporting Information).

Despite this, we continue to face several unresolved key issues: i) Spin-coating techniques do not allow for precise control over nanometer-scale thickness. ii) Fluctuations in the thickness of NPLs frequently cause mode hopping during testing, preventing stable single-mode output. Additionally, we have demonstrated that even minor thickness fluctuations of a few tens of nanometers in the NPLs can lead to accompanying peaks in the laser signal (Figure S6, Supporting Information). iii) As the thickness of the gain layer reduces to hundreds of nanometers, the lasing threshold for the FP mode increases, ultimately preventing continuous-wave pumping. As shown in Figure S7 (Supporting Information), in the laser with NPLs thickness at ≈750 nm, only spontaneous emission is observed.

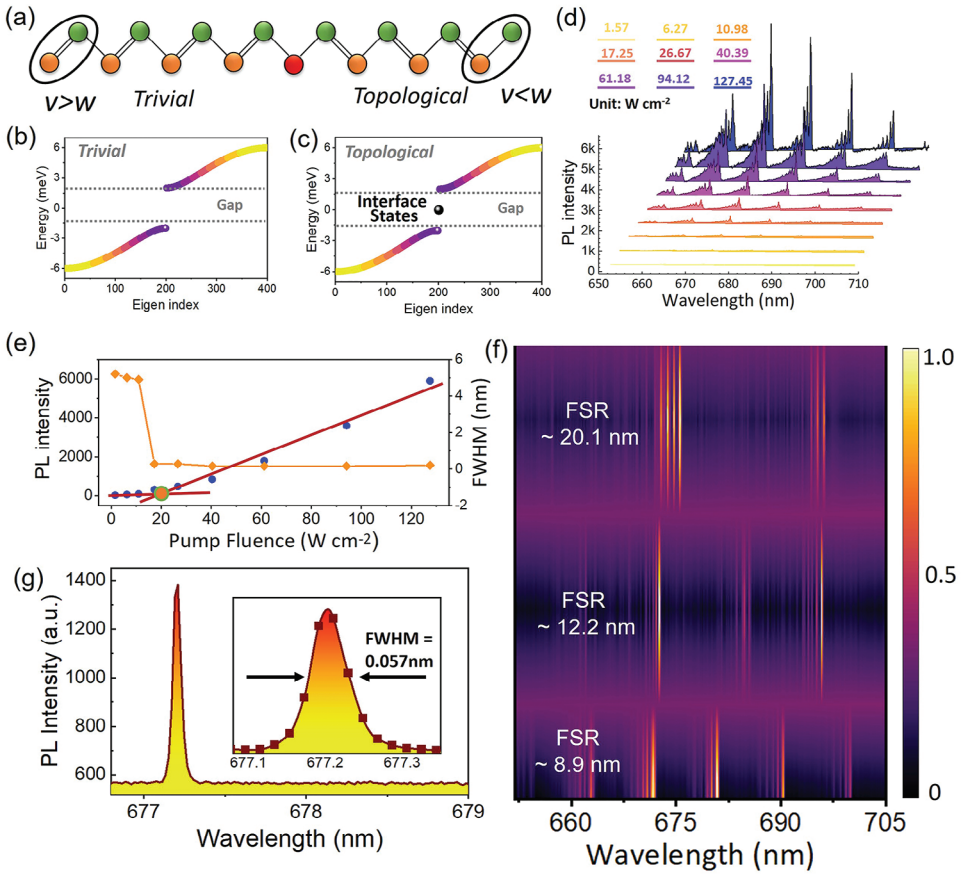

Figure 3. a) Schematic diagram illustrating a 1D chain formed by interfacing a trivial lattice and a topological lattice. b,c) Band structures of the designed 1D topological cavity. When the trivial lattice is put in contact with the topological lattice, the edge state emerges at their interface. In the photonic crystals we design, the calculated band structures for the LPC and UPC are identical albeit having different winding numbers. d) Power-dependent emission spectra of the topological vertical-cavity laser. e) Evolution of both normalized PL intensity and the FWHM of emission peaks from the lasers, characterized as functions of varying pump fluences. f) Lasing outputs in multi-mode configurations, demonstrating a range of FSRs. g) Single-mode lasing output with a FWHM of 0.057 nm, exhibiting a lasing Q-factor of ≈11 800.

2.4. CW Pumped Self-Assembled Colloidal Topological Laser

We studied the lasing properties and tunability of self-assembled NPLs layers at different nanoscale thicknesses, providing a concise schematic diagram (**Figure** 4a). A topological laser with an NPLs thickness of ≈100 nm was first investigated. This self-assembled 100 nm NPL layer consists of two distinct components: a 45 nm thick NPL layer that effectively replaces the half-layer of SiO_2 from the first unit cell of the UPC, complemented by an additional 55 nm thickness (Δd) contributed by NPLs. As shown in Figure S8 (Supporting Information), our measurements demonstrate that as the CW pumping power increases from 46 to 67 W cm^{-2}, the topological laser displays significant lasing behavior. This is highlighted by a dramatic narrowing of the FWHM from ≈24.5 to ≈2.3 nm. Furthermore, the distinct increase in the brightness of the laser spot with increasing pump power further confirms the onset of lasing behavior. By analyzing the relationship between emission intensity and pump fluence, we determined the lasing threshold for the NPLs – topological laser to be ≈56.4 W cm^{-2}, as depicted in Figure 4b. The positions of the topological modes measured closely aligns with theoretical simulation results, being 656.70 nm (experimental) and 656.44 nm (theoretical), as shown in Figure S9 (Supporting Information). With a continuous increase in NPL thickness, the topological interface states gradually evolve into first-order FP states. Interestingly, despite the first-order FP state laser featuring a gain layer nearly three times thicker than that of the topological interface state, both simulation and experimental results show that its Q-factor is lower than the topological mode's (Figure S9, Supporting Information). This highlights the superior performance and innovative design of our topological laser. Furthermore, the optical confinement factor of the topological interface mode is significantly higher than that of the Tamm mode formed in a cavity composed of two trivial photonic crystals, as shown in Figure S10 (Supporting Information). A high optical confinement factor is particularly important for enhancing laser efficiency, reducing the lasing threshold, and achieving continuous-wave laser output.

Generally, the semiconductor materials vertically stacked in cavity exhibits non-uniformity, causing various interfaces and scattering centers inside. This results in the randomization of the polarization direction of emission. Additionally, for colloidal NPLs, their random arrangement results in a random distribution of dipole moments, further exacerbating the non-polarized

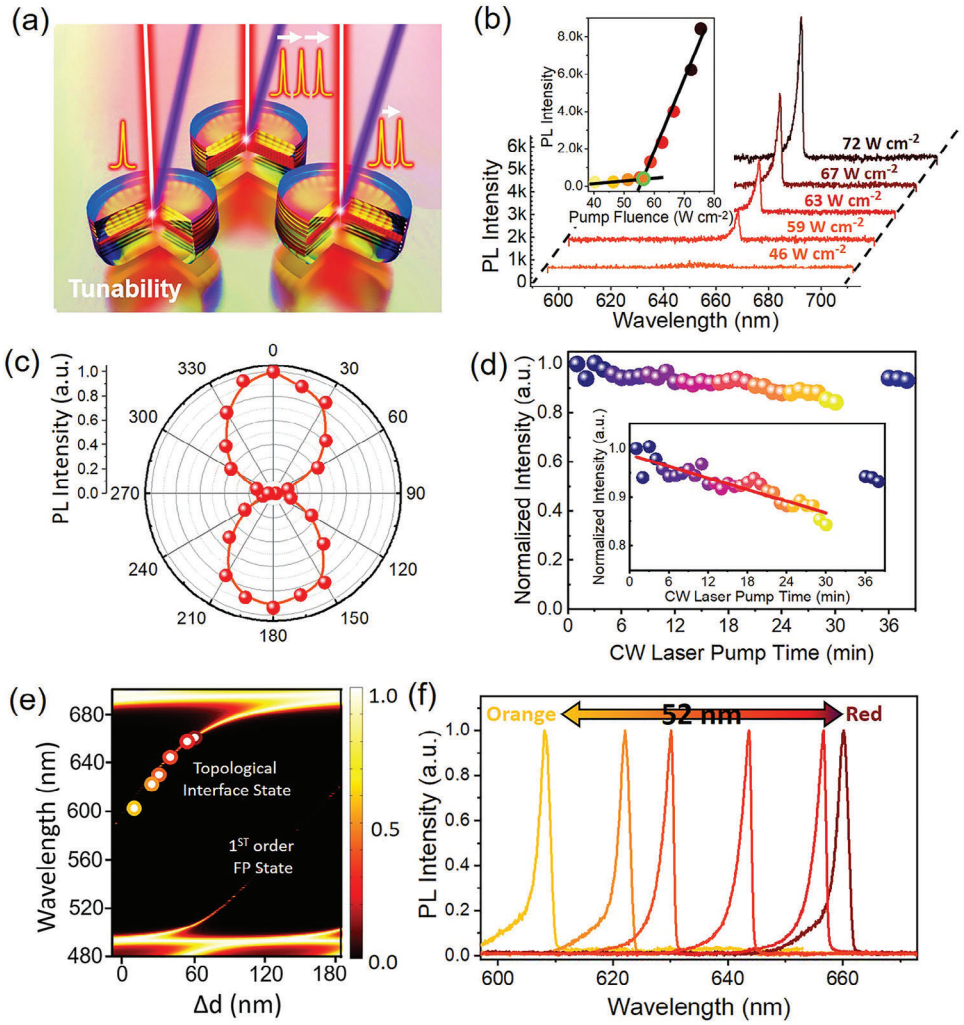

Figure 4. a) Schematic diagram of CW-pumped topological vertical-cavity with varying NPLs thickness. By changing the self-assembly thickness of NPLs, the tuning of the emitted lasing can be achieved. b) Power-dependence of the laser under CW pumping at room temperature. c) Polar plot of peak intensity versus the detection polarization angle. d) Stability testing under high-intensity (≈10 Pth) CW pumping. e) Emission spectra of the topological laser calculated theoretically as a function of the thickness of NPLs. f) Tunable single-mode lasing emission. ≈54 nm, and ≈60 nm. From left to right, the corresponding changes in NPL thicknesses are ≈11, ≈25, ≈31, ≈40, ≈54, and ≈60 nm. The emission wavelengths of topological lasers with these varying NPL thicknesses are marked in e).

nature of the emission. Here, we address this challenge by employing interface self-assembly strategies to form uniformly thick films, while also controlling the dipole distribution of NPLs. To delve into the polarization-dependent attributes of our NPLs-topological lasers, we meticulously analyzed the output laser intensity across varying rotation angles of a linear polarizer. The results, showcased in Figure 4c, reveal a high polarization degree—more than 95.7% according to Malus's law—indicating that our topological lasers produce a highly linearly polarized output. Moreover, the durability of these topological lasers under rigorous conditions was thoroughly assessed. Beyond the laser threshold, the photostability of the lasers was examined, as depicted in Figure 4d. Remarkably, after a 30 min test duration, the decrease in output lasing intensity was less than 18%. Interestingly, upon cessation of the pumping and following a brief 5 min cooling period, the laser's output power remarkably recovered to ≈95% of its initial level. This resilience suggests that the primary cause of performance degradation during the test was thermal effects, rather than any irreversible structural or material damage due to the high-intensity pumping. Such robustness demonstrated paves the way for utilizing colloidal lasers in scenarios demanding high power and extended operation durations.

In our uniquely designed topological cavity, the laser's emission wavelength exhibits remarkable flexibility, being tunable through adjustments in the self-assembled NPLs thickness, thus facilitating topological single-mode laser tuning, as evidenced in Figure 4e. To broaden the range of tuning capabilities, we have further synthesized orange-emitting CdSe/$Cd_{1-x}Zn_xS$ core/thin-shell NPLs with a PL emission centered at ≈604 nm (Figure S11, Supporting Information). As showcased in Figure 4f, by modulating the thickness of the mixed NPL films within a range of ≈49 nm (Δd ranging from ≈11 to 60 nm), we achieved an

impressive laser wavelength tuning from 608.21 to 660.23 nm, covering a span of over 52 nm. The tuned emission wavelengths are also marked in Figure 4e, illustrating the consistency between the experimental results and theoretical simulations. To our knowledge, this marks a pioneering achievement in achieving CW tuning across such a broad visible range in the domain of topological lasers. This milestone not only demonstrates the versatile and dynamic nature of our topological laser technology but also establishes a solid foundation for its practical application, particularly in domains necessitating precise, flexible, and stable wavelength control within the visible spectrum.

3. Conclusion

In summary, we have successfully realized self-assembled colloidal topological lasers in visible spectrum under CW pumping at room temperature. By exploiting the novel orientated alignment with fine thickness control and anisotropic dipole transition, our topological lasers demonstrate stable single-mode operation, offer considerable tunability and a high degree of polarization. Besides overcoming the fabrication challenges of topological lasers in the visible wavelength range, these achievements mark an important step toward the practical application of topological lasers. They not only pave the way to more accessible and cost-efficient laser production methods but also establish a foundation for the expanded use of colloidal NPLs in high-performance photonic devices. Looking ahead, our focus will shift toward refining these laser technologies for broader applications, emphasizing scalability and thermal management. This future direction is aimed at unlocking their full potential in cutting-edge photonic devices, further propelling the field into a new era of innovation and application.

4. Experimental Section

Preparation of Self-Assembled Colloidal Topological Lasers: In the fabrication process of self-assembled colloidal topological lasers, the initial step involved positioning a thoroughly cleaned, specially designed topological distributed Bragg reflector (DBR) mirror within a well-crafted from Teflon well. Then, alkane solution of NPLs was rapidly dropped onto the subphase surface. The added NPLs spread on the subphase surface, and the temperature of the experimental environment was controlled to remain constant. Following the complete evaporation of alkane, the subphase was gradually drained through a needle, allowing for the transfer of a tightly packed, uniformly oriented NPLs thin film onto the surface of the DBR. For multilayered deposition, this process was repeated onto previously deposited substrates as many times as needed. After this self-assembly procedure, it is necessary to carefully bond another complementary topological DBR mirror. This bonding was achieved by strategically applying optical glue along the periphery and pressing firmly to ensure robust and even contact with the NPLs film. For self-assembly of NPLs, please see Figures S2 and S12 (Supporting Information) for more details.

Lasing Measurement and Setup: A custom-built micro-photoluminescence (μ-PL) system was utilized to investigate the lasing behaviors of NPLs-topological lasers. For the CW pumped lasers, a He-Cd laser emitting at 442 nm was used. Samples were positioned on a 3D translation stage of an optical microscope. Optical signals were collected from the top of these devices using a 50x long working distance lens. These optical signals from the lasers were then either transmitted to a camera for PL imaging or channeled to a spectrometer. This spectrometer was equipped with a silicon charge-coupled device (CCD) camera, offering a spectral resolution of ≈0.043 nm/≈0.019 nm for detailed spectral recording and analysis.

Numerical simulation: The band structures for SSH model were calculated by MATLAB. Simulations for the transmission spectra and the spatial electric field distribution were performed in the Electromagnetic Waves, Frequency Domain (ewfd) module with COMSOL Multiphysics, a commercial software based on the Finite Element Method. A 2D geometry was exploited for which the x-axis was chosen as the stacking direction and the y-axis represented an arbitrary direction parallel to the surface of layers. Periodic boundary conditions were applied along the x-axis on the top and bottom boundaries of the simulated geometry. A plane-wave source was placed at the left boundary and the transmission is detected at the right boundary. Parametric Sweep was applied to wavelength and NPLs thickness in the simulation.

The Factor of the Polarization: The polarization anisotropy can be quantitatively calculated from the factor of the polarization state defined as:[1,36]

$$R = \frac{I_{max} - I_{min}}{I_{max} + I_{min}} \tag{3}$$

where I_{max} and I_{min} correspond to the maximum and minimum lasing emission intensity, respectively.

Supporting Information

Supporting Information is available from the Wiley Online Library or from the author.

Acknowledgements

This work was supported by the Singapore National Research Foundation Competitive Research Program grant NRF-CRP23-2019-0007 and Singapore Ministry of Education Academic Research Fund Tier 1 grant RG139/22. H.D.S. acknowledges the support from CPG2024-00006, SRG2023-00025, and the Science and Technology Development Fund (FDCT), Macao SAR (File no. 0122/2023/RIA2). Q.Z. acknowledges the support from National Natural Science Foundation of China No. 12104318. The authors thank Dr. Z.Y. Liu from the Photonics Center of Shenzhen University for technical support. T.Y. gratefully acknowledges the strong support provided by the Presidential Postdoctoral Fellowship at Nanyang Technological University, award number: 022430-00001. Z.Z. gratefully acknowledges the support provided by the Guangdong Academy of Sciences' Project of Science and Technology Development at Guangdong Academy of Sciences, award number: 2022GDASZH-2022010107. H.V.D. gratefully acknowledge the financial support from the Scientific and Technological Research Council of Türkiye (TUBITAK), grant number 121C266 and TUBA – Turkish Academy of Sciences.

Conflict of Interest

The authors declare no conflict of interest.

Author Contributions

R.D., Q.Z., and Y.T.T. contributed equally to this work. H.D.S. and B.L.Z. initialized this research. R.D. and Q.Z. designed and discussed the experiments. R.D., Q.Z., Y.T.T., T.Y., X.Z., and T.R. performed the optical characterization experiments. Y.T.T., L.X., Z.T.Z., and H.V.D. contributed to the fabrication of nanoplatelets. R.D., C.X.X.L., and W.S.L. conducted and interpreted the atomic force microscopy. Q.Z. and R.D. did the theoretical simulation. R.D., Q.Z., B.L.Z., and H.D.S. analyzed the data. R.D., Q.Z., and Y.T.T. drafted the manuscript. H.D.S. and B.L.Z. supervised the research and revised the manuscript.

Data Availability Statement

The data that support the findings of this study are available from the corresponding author upon reasonable request.

Keywords

colloidal nanoplatelets, continuous-wave pumping, self-assembled topological laser, wavelength tunability

Received: October 30, 2024
Revised: December 30, 2024
Published online: February 7, 2025

[1] R. Duan, Z. Zhang, L. Xiao, X. Zhao, Y. T. Thung, L. Ding, Z. Liu, J. Yang, V. D. Ta, H. D. Sun, *Adv. Mater.* **2022**, *34*, 2108884.
[2] Y. T. Thung, R. Duan, E. G. Durmusoglu, Y. He, L. Xiao, C. X. X. Lee, W. S. Lew, L. Zhang, H. V. Demir, H. D. Sun, *Laser Photonics Rev.* **2023**, *17*, 2200849.
[3] R. Duan, Y. T. Thung, Z. Zhang, E. G. Durmusoglu, Y. He, L. Xiao, L. Zhang, H. Li, J. Yang, H. V. Demir, H. D. Sun, *Laser Photonics Rev.* **2023**, *18*, 2300745.
[4] J. Q. Grim, S. Christodoulou, F. Di Stasio, R. Krahne, R. Cingolani, L. Manna, I. Moreels, *Nat. Nanotech.* **2014**, *9*, 891.
[5] Z. Yang, M. Pelton, I. Fedin, D. V. Talapin, E. Waks, *Nat. Commun.* **2017**, *8*, 143.
[6] O. Erdem, S. Foroutan, N. Gheshlaghi, B. Guzelturk, Y. Altintas, H. V. Demir, *Nano Lett.* **2020**, *20*, 6459.
[7] Y. Gao, M. C. Weidman, W. A. Tisdale, *Nano Lett.* **2017**, *17*, 3837.
[8] R. Momper, H. Zhang, S. Chen, H. Halim, E. Johannes, S. Yordanov, D. Braga, B. Blülle, D. Doblas, T. Kraus, M. Bonn, H. I. Wang, A. Riedinger, *Nano Lett.* **2020**, *20*, 4102.
[9] H. D. Baruj, I. Bozkaya, B. Canimkurbey, A. T. Isik, F. Shabani, S. Delikanli, S. Shendre, O. Erdem, F. Isik, H. V. Demir, *Small* **2023**, *19*, 2206582.
[10] J. Ye, A. Ren, L. Dai, T. K. Baikie, R. Guo, D. Pal, S. Gorgon, J. E. Heger, J. Huang, Y. Sun, R. Arul, G. Grimaldi, K. Zhang, J. Shamsi, Y. Huang, H. Wang, J. Wu, A. F. Koenderink, L. Torrente Murciano, M. Schwartzkopf, S. V. Roth, P. Mller-Buschbaum, J. J. Baumberg, S. D. Stranks, N. C. Greenham, L. Polavarapu, W. Zhang, A. Rao, R. L. Z. Hoye, *Nat. Photon.* **2024**, *18*, 586.
[11] S. Ithurria, M. D. Tessier, B. Mahler, R. P. S. M. Lobo, B. Dubertret, *Nat. Mater.* **2011**, *10*, 936.
[12] M. D. Tessier, C. Javaux, I. Maksimovic, V. Loriette, B. S. Dubertret, *ACS Nano* **2012**, *6*, 6751.
[13] M. Olutas, B. Guzelturk, Y. Kelestemur, A. Yeltik, S. Delikanli, H. V. Demir, *ACS Nano* **2015**, *9*, 5041.
[14] P. Geiregat, C. Rodá, I. Tanghe, S. Singh, A. Di Giacomo, D. Lebrun, G. Grimaldi, J. Maes, D. Van Thourhout, I. Moreels, A. J. Houtepen, Z. Hens, *Light: Sci. Appl.* **2021**, *10*, 112.
[15] J. Yu, S. Hou, M. Sharma, L. Y. M. Tobing, Z. Song, S. Delikanli, C. Hettiarachchi, D. Zhang, W. Fan, M. D. Birowosuto, H. Wang, H. V. Demir, C. Dang, *Matter* **2020**, *2*, 1550.
[16] B. Guzelturk, M. Pelton, M. Olutas, H. V. Demir, *Nano Lett.* **2019**, *19*, 277.
[17] F. Fan, O. Voznyy, R. P. Sabatini, K. T. Bicanic, M. M. Adachi, J. R. McBride, K. R. Reid, Y. S. Park, X. Li, A. Jain, R. Quintero-Bermudez, M. Saravanapavanantham, M. Liu, M. Korkusinski, P. Hawrylak, V. I. Klimov, S. J. Rosenthal, S. Hoogland, E. H. Sargent, *Nature* **2017**, *544*, 75.
[18] Y. S. Park, J. Roh, B. T. Diroll, R. D. Schaller, V. I. Klimov, *Nat. Rev. Mater.* **2021**, *6*, 382.
[19] L. Lu, J. D. Joannopoulos, M. Soljačić, *Nat. Photonics* **2014**, *8*, 821.
[20] T. Ozawa, H. M. Price, A. Amo, N. Goldman, M. Hafezi, L. Lu, M. C. Rechtsman, D. Schuster, J. Simon, O. Zilberberg, I. Carusotto, *Rev. Mod. Phys.* **2019**, *91*, 015006.
[21] M. A. Bandres, S. Wittek, G. Harari, M. Parto, J. Ren, M. Segev, D. N. Christodoulides, M. Khajavikhan, *Science* **2018**, *359*, eaar4005.
[22] P. St-Jean, V. Goblot, E. Galopin, A. Lemaître, T. Ozawa, L. Le Gratiet, I. Sagnes, J. Bloch, A. Amo, *Nat. Photonics* **2017**, *11*, 651.
[23] C. Han, M. Lee, S. Callard, C. Seassal, H. Jeon, *Light: Sci. Appl.* **2019**, *8*, 40.
[24] H.-R. Kim, M.-S. Hwang, D. Smirnova, K.-Y. Jeong, Y. Kivshar, H.-G. Park, *Nat. Commun.* **2020**, *11*, 5758.
[25] W. Zhang, X. Xie, H. Hao, J. Dang, S. Xiao, S. Shi, H. Ni, Z. Niu, C. Wang, K. Jin, X. Zhang, X. Xu, *Light: Sci. Appl.* **2020**, *9*, 109.
[26] Y. Zeng, U. Chattopadhyay, B. Zhu, B. Qiang, J. Li, Y. Jin, L. Li, A. G. Davies, E. H. Linfield, B. Zhang, Y. Chong, Q. J. Wang, *Nature* **2020**, *578*, 246.
[27] L. Yang, G. Li, X. Gao, L. Lu, *Nat. Photonics* **2022**, *16*, 279.
[28] J. Tian, Q. Y. Tan, Y. Wang, Y. Yang, G. Yuan, G. Adamo, C. Soci, *Nat. Commun.* **2023**, *14*, 1433.
[29] J. Wu, S. Ghosh, Y. Gan, Y. Shi, S. Mandal, H. Sun, B. Zhang, T. C. H. Liew, R. Su, Q. Xiong, *Sci. Adv.* **2023**, *9*, eadg4322.
[30] Y. Wang, X. Li, J. Song, L. Xiao, H. Zeng, H. D. Sun, *Adv. Mater.* **2015**, *27*, 7101.
[31] A. Palatnik, M. Sudzius, S. Meister, K. Leo, *Nanophotonics* **2021**, *10*, 2459.
[32] X. M. Gao, X. Y. Liu, Y. Yang, B. Shi, J. Wu, L. Lu, Z. Wang, *Nat. Nanotechnol.* **2020**, *15*, 1012.
[33] A. J. Heeger, S. Kivelson, J. R. Schrieffer, W. P. Su, *Rev. Mod. Phys.* **1988**, *60*, 781.
[34] J. Zak, *Phys. Rev. Lett.* **1989**, *62*, 2747.
[35] M. Xiao, Z. Q. Zhang, C. T. Chan, *Phys. Rev. X* **2014**, *4*, 021017.
[36] J. Hu, L. Li, W. Yang, L. Manna, L. Wang, A. P. Alivisatos, *Science* **2001**, *292*, 2060.